Atmos. Chem. Phys., 24, 6495–6508, 2024
https://doi.org/10.5194/acp-24-6495-2024

Atmospheric Chemistry and Physics
Open Access
EGU

Daytime and nighttime aerosol soluble iron formation in clean and slightly polluted moist air in a coastal city in eastern China

Wenshuai Li[1,2], Yuxuan Qi[1,2], Yingchen Liu[1,2], Guanru Wu[1,2], Yanjing Zhang[1,2], Jinhui Shi[3], Wenjun Qu[1,2], Lifang Sheng[1,2], Wencai Wang[1,2], Daizhou Zhang[4], and Yang Zhou[1,2]

[1]Frontier Science Center for Deep Ocean Multispheres and Earth System (FDOMES) and Physical Oceanography Laboratory, Ocean University of China, Qingdao 266100, China
[2]College of Oceanic and Atmospheric Sciences, Ocean University of China, Qingdao 266100, China
[3]College of Environmental Science and Engineering, Ocean University of China, Qingdao 266100, China
[4]Faculty of Environmental and Symbiotic Sciences, Prefectural University of Kumamoto, Kumamoto 862-8502, Japan

Correspondence: Daizhou Zhang (dzzhang@pu-kumamoto.ac.jp) and Yang Zhou (yangzhou@ouc.edu.cn)

Received: 15 November 2023 – Discussion started: 6 December 2023
Revised: 31 March 2024 – Accepted: 15 April 2024 – Published: 4 June 2024

Abstract. Photocatalytic reactions during the daytime, alongside aqueous-phase reactions occurring during both daytime and nighttime, are identified as the two primary processes facilitating the conversion of aerosol iron (Fe) from the insoluble state to the soluble state within the atmospheric environment. This study investigated the levels of total Fe (Fe_T) and soluble Fe (Fe_S) in $PM_{2.5}$ samples collected during daytime and nighttime in Qingdao, a coastal city in eastern China, evaluating the distinctive roles of these two pathways in enhancing aerosol Fe solubility (%Fe_S, defined as the ratio of Fe_S to Fe_T). Under clean and humid conditions, characterized by prevailing sea breezes and a relative humidity (RH) typically above 80 %, an average daytime %Fe_S of 8.7 % was observed, which systematically exceeded the nighttime %Fe_S (6.3 %). Photochemical conversions involving oxalate contributed to the higher %Fe_S observed during daytime. Conversely, in scenarios where air masses originated from inland areas and exhibited slightly polluted, daytime %Fe_S (3.7 %) was noted to be lower than the nighttime %Fe_S (5.8 %). This discrepancy was attributable to the variations in RH, with nighttime RH averaging around 77 %, conducive to the more efficient generation of acidic compounds, thereby accelerating Fe_S production compared to the daytime, when RH was only about 62 %. Furthermore, the oxidation rates of sulfur (SOR) displayed a strong correlation with RH, particularly when RH fell below 75 %. A 10 % increase in RH corresponded to a 7.6 % rise in SOR, which served as the primary driver of the higher aerosol acidity and %Fe_S at night. These findings highlight the RH-dependent activation of aqueous-phase reactions and the augmentation of daytime photocatalysis in the formation of Fe_S in the coastal moist atmosphere.

1 Introduction

Iron (Fe) plays a pivotal role as a micronutrient in marine ecosystems, being a critical component of atmospheric aerosol particles (Martin et al., 1994). Its deposition in high-nitrate, low-chlorophyll (HNLC) regions can trigger phytoplankton bloom, thus enhancing atmospheric carbon absorption and fixation in seawater (Watson et al., 1994; Watson and Lefévre, 1999; Toner, 2023). Notably, only the soluble fraction of Fe (Fe_S) in aerosols, referred to as bioavailable Fe, is accessible to phytoplankton (Zhuang et al., 1992; Sugie et al., 2013; Li et al., 2017). The proportion of Fe_S to the total aerosol Fe (Fe_T), i.e., the aerosol Fe solubility (%Fe_S), is influenced by the aerosols' sources and the chemical conversion of Fe from insoluble forms to soluble forms in the atmosphere. %Fe_S in fresh dust particles is typ-

ically below 1 %, but it can exceed 10 % in aerosols derived from combustion processes, such as fly ash from coal and oil combustion (Oakes et al., 2012; Shi et al., 2012; Wang et al., 2015; Li et al., 2022). The $\%Fe_S$ in primary particles can significantly increase due to atmospheric processes, primarily through aerosol acidification via aqueous-phase reactions or photochemical conversions of precursors of acidic species (Solmon et al., 2009; Shi et al., 2015; Li et al., 2017; Hettiarachchi et al., 2019), affecting the deposition flux of aerosol Fe_S over the open ocean (Chen and Siefert, 2004; Shi et al., 2013; Yang et al., 2020).

Solar radiation and ambient humidity are two key meteorological factors that greatly influence the processes of aerosol acidification. Solar irradiation induces photochemical reactions during daytime, leading to the formation of free radicals and accelerating the production of acidic species within aerosols, thereby facilitating Fe dissolution (Chen and Grassian, 2013; T. Liu et al., 2021). Studies such as Fu et al. (2010) have demonstrated increased Fe_S in dust samples exposed to light in the HCl solution. Furthermore, daytime photolysis of Fe-organic complexes is another pathway for Fe_S formation, contributing to increased $\%Fe_S$ (Weller et al., 2014; Zhang et al., 2019; Zhou et al., 2020). For example, Zhou et al. (2020) and Zhang et al. (2019) reported that photolysis of oxalate-Fe(III) complex can result in the degradation of oxalate, enhancing Fe dissolution in aerosol particles during daytime. These mechanisms have been supported by laboratory experiments and model simulations (Zhu et al., 1993; Chen and Grassian, 2013; Sorooshian et al., 2013; Pang et al., 2019; Li et al., 2021). In contrast, high ambient relative humidity (RH) can facilitate the heterogeneous and liquid-phase formation of sulfate and nitrate during nighttime, increasing aerosol acidity and promoting acid-associated Fe dissolution (Liu et al., 2020; Pye et al., 2020; Wong et al., 2020). Studies like Zhang et al. (2022) observed enhanced $\%Fe_S$ ($> 1\,\%$) at high RH levels ($> 60\,\%$) in winter, while Zhu et al. (2020) highlighted the greater impact of SO_4^{2-} and NO_3^- on $\%Fe_S$ at RH above 50 %. Shi et al. (2020) noted efficient Fe_S formation under foggy conditions, where SO_4^{2-} and NO_3^- concentrations were high due to the absorption of precursor gases on wet particle surfaces, facilitating further water vapor absorption and Fe_S increase.

Aqueous-phase processes can occur during both daytime and nighttime, given adequate moisture. The formation of Fe_S results from the interplay between photochemistry and aqueous chemistry during daytime, whereas it relies solely on aqueous chemistry at night. The synergistic mechanisms and their individual contributions to Fe_S formation remain partially understood.

To elucidate the roles of aqueous-phase and photochemical reactions on Fe_S formation, we collected $PM_{2.5}$ samples during daytime and nighttime separately in a Chinese coastal city (Qingdao). Positioned under the westerlies of the Northern Hemisphere, Qingdao acts as a primary conduit for East Asian terrestrial aerosols to the northwestern Pacific. Our research focuses on ascertaining the $\%Fe_S$ enhancement under clean and slightly polluted air conditions, reflecting typical coastal air quality. The primary goal is to delineate the contributions of aqueous-phase reactions and photochemical processes to $\%Fe_S$ enhancement, thereby elucidating the dynamics of Fe dissolution within the atmospheric chemistry of coastal areas.

2 Methodology and materials

2.1 Sample collection and classification

The observation was carried out on the following dates: 24 April to 27 May 2017; 28 March to 30 April 2018; and 22 to 28 May 2018. Two high-volume $PM_{2.5}$ samplers (TISCH, TE-6070BLX-2.5, USA) were applied to collect $PM_{2.5}$ onto quartz microfiber filters (QM-A, PALL) and Whatman® 41 filters, respectively, on the roof of Baguanshan Atmospheric Research Observatory (BARO, 36°03′ N, 120°20′ E, 76 m a.s.l.). BARO is located on the top of a small hill in the urban area of Qingdao and around 0.7 km away from the coastline of the Yellow Sea (Fig. S1 in the Supplement). $PM_{2.5}$ samples were collected separately during daytime and nighttime. Field blank samples were also collected during the campaign by placing filters in the samplers with the samplers switched off. After the sampling process, $PM_{2.5}$ samples were sealed and stored at −20 °C before analysis.

For the measurement of water-soluble ions (WSIs) and carbonaceous matters, aerosol samples collected on QM-A filters were utilized. The samples collected on Whatman® 41 filters were used for the detection of elements. Firstly, samples were cut into pieces and immersed in Milli-Q pure water. Then, water-soluble matters were extracted by ultrasonic vibration at approximately 0 °C for 40 min. The water extracts were then filtered through syringes with 0.45 µm strainer heads (PALL). The filtered extracts were analyzed for WSIs, including Na^+, NH_4^+, K^+, Mg^{2+}, Ca^{2+}, F^-, Cl^-, SO_4^{2-}, NO_3^-, and $C_2O_4^{2-}$, using ion chromatography (IC, Dionex ICS-3000, Dionex Corp., Sunnyvale, CA, USA). Similar sample pretreatment procedures were used to determine soluble elements. While 10 mL of filtrate was taken and 0.187 mL HNO_3 (mass fraction: 69 %) was added to water extracts before measuring soluble elements, in this case soluble Fe(II) was oxidized into an insoluble state. To determine total elements, sample pieces were placed into inner tanks and subjected to digestion with a mixture of $HNO_3 + HF$ (at a volume ratio of 4 : 1) at 180 °C for 48 h. The element concentrations were measured using inductively coupled plasma mass spectrometry (ICP-MS; model: iCAP Qc, Thermo Fisher Scientific Inc., Germany). Carbonaceous materials, specifically organic carbon (OC) and elemental carbon (EC), were analyzed using a sunset OC/EC analyzer from Sunset Laboratory Inc. The detection limits of the analysis instruments used can be found in Table S1. The organic matter (OM) content was estimated with 1.6× OC, as

proposed by Turpin and Lim (2001). Further details about sample collection, pretreatment procedures, and chemical species detection can be found in our previous work (Li et al., 2023a, b).

Various weather conditions and air pollution characteristics were encountered during the observation period, including clean, slightly polluted (SP), heavily polluted, foggy, and dusty conditions. Due to the large deviations and uncertainties in the statistical results of dust-related samples, data from these samples were not considered. Additionally, samples from heavily polluted periods ($N = 6$, defined by $PM_{2.5} > 50\,\mu g\,m^{-3}$ and $PM_{2.5}/PM_{10} > 0.4$) and fog-influenced samples ($N = 12$) were also not included because of the limited sample number and the significant difference in fog durations between samples. In this paper, we focus on the results of the clean period samples ($N = 19$) and the SP period samples ($N = 32$). Clean periods samples were collected when $PM_{2.5} < 30\,\mu g\,m^{-3}$ and $PM_{10} < 50\,\mu g\,m^{-3}$. The SP periods samples were those collected when $30\,\mu g\,m^{-3} < PM_{2.5} < 50\,\mu g\,m^{-3}$ and those collected when $PM_{2.5} < 30\,\mu g\,m^{-3}$ while $PM_{10} > 50\,\mu g\,m^{-3}$.

2.2 Aerosol pH and liquid water content

The ISORROPIA thermodynamic equilibrium model (version II, https://www.epfl.ch/labs/lapi/models-and-software/isorropia/iso-code-repository/, last access: 17 April 2024) was employed to estimate gas concentrations and aerosol water pH (Song et al., 2018). The forward mode, which uses both gas and aerosol data as model input, was utilized for pH calculations. This approach was preferred over the reverse mode because the latter, using only aerosol data, is very sensitive to the uncertainties of the measured WSIs concentrations (Hennigan et al., 2015; Song et al., 2018). "Metastable-mode" was employed in ISORROPIA, assuming that solid precipitates did not form except for $CaSO_4$. The concentrations of gaseous species (i.e., NH_3(g), HNO_3(g), HCl(g)) were not measured at the site. In alignment with the approach proposed by Sun et al. (2018), we devised a strategy to estimate the concentrations of these gaseous species. Initially, the input of aerosol data was assumed as the sum of aerosol and gas data (specifically for HNO_3, HCl, and NH_3). This step provided us with the first set of gas and aerosol data outputs. For the second run, the gas data output derived from the initial run was added to the original aerosol data, and it was considered as the sum of gas data and aerosol data just like the first run to calculate HNO_3(g), HCl(g) and NH_3(g). The same method was employed for subsequent iterations until the variance in the NO_3^- output below the 1 % threshold in mass. The calculation processes can be described by the following equations:

$$\mathrm{Input}[C_{\mathrm{Aerosol}} + C_{\mathrm{Gas}}]_{N+1} = C_{\mathrm{Aerosol}} + [C_{\mathrm{Gas}}]_{\mathrm{N}}, \quad (1)$$

$$L = \left| \frac{\left[C_{NO_3^-}\right]_{N+1} - \left[C_{NO_3^-}\right]_{\mathrm{N}}}{\left[C_{NO_3^-}\right]_{\mathrm{N}}} \right| \times 100\,\%, \quad (2)$$

where C_{Aerosol} is the observed concentration of NO_3^- (or NH_4^+, Cl^-), C_{Gas} is the concentration of gaseous species of HNO_3(g) (or NH_3(g), HCl(g)), and $[C_{\mathrm{Gas}}]_{\mathrm{N}}$ is the concentration of gaseous species of HNO_3(g) (or NH_3(g), HCl(g)) output by ISORROPIA in the Nth run ($N \geq 1$). The iteration was stopped until $L < 1\,\%$.

Finally, iterations were performed three times ($N_{\max} = 3$) to determined when $L = 0.1\,\%$. The aerosol pH was calculated using aqueous H^+ concentration and aerosol liquid water content (ALWC) output by ISORROPIA, as described by Eq. (3).

$$\mathrm{pH} = -\log_{10} \frac{1000 \times \mathrm{H}^+(\mathrm{aq})}{\mathrm{ALWC}} \quad (3)$$

Significant correlations between the results of the first run and the fourth run were observed for pH ($r^2 = 0.95$) and ALWC ($r^2 = 0.99$), indicating the stability and reliability in estimating the pH and ALWC by ISORROPIA II (Fig. S2). Moreover, the correlations of NO_3^- ($r^2 = 0.71$), NH_4^+ ($r^2 = 0.98$) and Cl^- ($r^2 = 0.51$) between the simulated results and measured concentrations are significant, demonstrating the robust confidence level of the simulated results (Fig. S3).

In addition, the impact of organic matter (OM) on aerosol pH was determined to be minimal. This can be attributed to the limited sensitivity of the predicted pH to the water uptake by organic species ($ALWC_{org}$) when the OM fraction in $PM_{2.5}$ is low (Guo et al., 2015; Liu et al., 2017). Following the methods of Guo et al. (2015), we estimated $ALWC_{org}$ and its influence on aerosol pH. Our analysis determined the $ALWC_{org}$ to range between 0.83 and $3.31\,\mu g\,m^{-3}$, constituting merely 2.6 %–9.8 % of the total ALWC. Aerosol pH was about 0.03–0.08 higher when considering OM, affirming the negligible effect of OM on aerosol pH (see Sect. S1 in the Supplement for more details).

2.3 Weather conditions and air quality data

The publicly released temperature, RH, surface pressure, wind speed, and wind direction recorded every 10 min were obtained from a meteorological observatory of the Qingdao Meteorological Bureau (Fig. S1). Hourly mass concentrations of $PM_{2.5}$, PM_{10}, SO_2, NO_2, O_3, and CO were obtained from an adjacent air quality monitoring station in the Shinan District of Qingdao City (Fig. S1), which is managed by Ministry of Ecology and Environment of the People's Republic of China (http://www.mee.gov.cn/, last access: 15 April 2024).

To examine the relative abundance of chemical species in aerosols, we reconstructed the mass concentrations of $PM_{2.5}$

by Eq. (4) using the obtained concentrations of WSIs, OM, EC, and elements.

$$PM_{2.5R} = WSIs + OM + EC + Elements + Si + Ca, \quad (4)$$

where $PM_{2.5R}$ is the reconstructed $PM_{2.5}$ and WSIs consists of Na^+, NH_4^+, K^+, F^-, Cl^-, SO_4^{2-}, NO_3^-, and $C_2O_4^{2-}$. As for elements, Mg, Al, V, Cr, Mn, Fe, Ni, Co, Cu, Zn, Ga, As, Se, Rb, Sr, Cd, Ba, Tl, and Pb were considered. Si and Ca concentrations were estimated based on the mass ratio of Si/Al (3.43) following the methodology described by Huang et al. (2010) and the mass ratio of Ca/Al (0.80) suggested by Arimoto et al. (2004) and Wang et al. (2011). Because the nearby monitoring station is closer to the sea and less affected by human activities (yellow dot in Fig. S1), the level of $PM_{2.5R}$ is higher than the observations from the monitoring station. However, the trends in the variations of these two datasets were consistent, indicating the high confidence of the $PM_{2.5R}$ dataset. In addition, any mention of ionic ratios or normalized parameters in the results and discussions of this paper indicates the data were divided by $PM_{2.5R}$.

2.4 Provenance of air masses

The HYbrid Single-particle Lagrangian Integrated Trajectory (HYSPLIT) Model (https://www.ready.noaa.gov/HYSPLIT.php, last access: 15 April 2024), developed by NOAA, was applied to calculate the origins of air masses from which $PM_{2.5}$ samples were collected. Gridded GDAS data with a horizontal resolution of $1.0° \times 1.0°$ were used as the input. Backward trajectories were computed for a period of 48 h, with starting points located at 300 m above ground level.

3 Results

3.1 Meteorological features of clean and SP periods

During clean periods, the backward trajectories reveal that the air masses mainly originated from sea areas (Fig. 1). The prevailing sea breeze resulted in high RH levels of 81.5 ± 4.9 % during daytime and 86.6 ± 8.8 % during nighttime (Table 1). The minimal temperature variance of about 2° between daytime and nighttime further reflects the characteristics of the marine atmosphere. In contrast, air masses during SP periods originated from various directions, with a significant number traversing terrestrial regions prior to arriving at the collection site. Temperature and RH exhibited noticeable diurnal variations. The daytime temperature was $17.2 \pm 3.0°$ and decreased to $13.2 \pm 3.7°$ during nighttime. The RH levels were 62.1 ± 9.4 % and 76.8 ± 9.4 % during daytime and nighttime, respectively.

3.2 Concentrations of $PM_{2.5}$ and Fe, and $\%Fe_S$

Table 1 presents the $PM_{2.5}$ levels and aerosol Fe concentrations during both clean and SP periods. Under clean conditions, $PM_{2.5}$ concentrations were similar during daytime and nighttime, with average values of 16.9 and 16.4 $\mu g\,m^{-3}$, respectively. Compared to the nighttime, Fe_T and Fe_S concentrations were higher during the daytime, which were $289.2 \pm 223.4\ ng\,m^{-3}$ and $20.0 \pm 10.5\ ng\,m^{-3}$, respectively. Daytime levels of Fe_T and Fe_S were 1.5 times and 1.6 times as high as those observed at night, respectively. The increase in Fe_T and Fe_S during daytime may be linked to heightened human activities. Furthermore, the elevated Fe_S during daytime could be attributed to photochemical processes, which promoted the dissolution of aerosol Fe, a topic to be discussed further in Sect. 4.2. $\%Fe_S$ values ranged from 2.3 % to 14.1 % with an average of 8.7 % during daytime, approximately 1.4 times the nighttime average of 6.3 % (after removing an extreme point of 37.2 %).

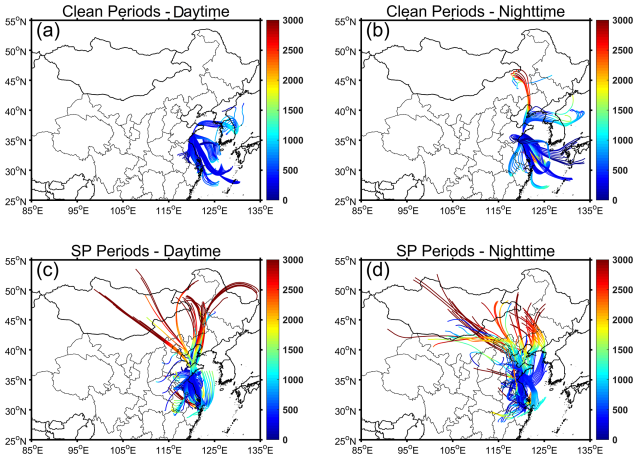

Figure 1. The 48 h backward trajectories during daytime and nighttime during clean and slightly polluted (SP) periods. Trajectories are color coded based on the altitude (unit: m) above the ground.

Under SP conditions, $PM_{2.5}$ was at similar levels during daytime and nighttime, with average values of 30.3 and 28.3 $\mu g\,m^{-3}$, respectively. However, the daytime Fe_T ($938.3 \pm 850.5\ ng\,m^{-3}$) was much higher than the nighttime Fe_T ($520.3 \pm 496.1\ ng\,m^{-3}$), which was approximately 3-fold higher than during clean periods. Similarly, the daytime Fe_S concentration of $25.7 \pm 10.5\ ng\,m^{-3}$ was also slightly higher than the nighttime concentrations of $21.6 \pm 8.1\ ng\,m^{-3}$, which was 1–2 times higher than that during the clean period. Different from the clean period, $\%Fe_S$ was markedly higher at night ($5.8\ \% \pm 3.0\ \%$) compared to the daytime $\%Fe_S$ ($3.7\ \% \pm 2.0\ \%$) during the SP period, ranging from 1.0 % to 12.3 %.

3.3 Chemical characteristics of $PM_{2.5}$

Figure 2 illustrates the mass fractions of various chemical species present in the reconstructed $PM_{2.5}$ ($PM_{2.5R}$). During the clean period, WSIs were the dominant components, constituting about 75.0 % and 74.1 % of $PM_{2.5}$ mass during daytime and nighttime, respectively. SO_4^{2-}, NO_3^-, and NH_4^+ were

Table 1. Meteorological parameters, $\%Fe_S$, aerosol pH, and concentrations (average ± standard deviation) of $PM_{2.5}$ and chemical species during clean and slightly polluted periods.

	Clean periods		Slightly polluted periods	
	Daytime	Nighttime	Daytime	Nighttime
$PM_{2.5}$ ($\mu g\,m^{-3}$)	16.9 ± 3.1	16.4 ± 5.6	30.3 ± 7.0	28.3 ± 7.7
Temperature (°)	16.6 ± 2.8	14.3 ± 2.3	17.2 ± 3.0	13.2 ± 3.7
RH (%)	81.5 ± 4.9	86.6 ± 8.8	62.1 ± 9.4	76.8 ± 9.4
ALWC ($\mu g\,m^{-3}$)	30.0 ± 13.5	55.0 ± 53.7	22.5 ± 13.2	44.1 ± 33.8
Fe_T ($ng\,m^{-3}$)	289.2 ± 223.4	186.7 ± 122.2	938.3 ± 850.5	520.3 ± 496.1
Fe_S ($ng\,m^{-3}$)	20.0 ± 10.5	12.5 ± 7.4	25.7 ± 10.5	21.6 ± 8.1
$\%Fe_S$ (%)	8.7 ± 3.8	6.3 ± 4.1	3.7 ± 2.0	5.8 ± 3.0
pH	0.46 ± 0.83	1.06 ± 0.96	1.16 ± 0.88	0.98 ± 0.75
SO_4^{2-} ($\mu g\,m^{-3}$)	13.97 ± 5.19	10.97 ± 8.06	14.94 ± 5.81	13.78 ± 5.43
$F(SO_4^{2-})$[a]	$42.9\,\% \pm 14.0\,\%$	$36.8\,\% \pm 14.0\,\%$	$20.9\,\% \pm 3.6\,\%$	$23.0\,\% \pm 5.3\,\%$
NO_3^- ($\mu g\,m^{-3}$)	5.82 ± 3.49	5.63 ± 4.87	26.71 ± 13.15	22.80 ± 10.81
$F(NO_3^-)$[b]	$15.7\,\% \pm 6.0\,\%$	$17.7\,\% \pm 11.3\,\%$	$35.4\,\% \pm 9.0\,\%$	$35.6\,\% \pm 9.0\,\%$
$(2[SO_4^{2-}]+[NO_3^-])/PM_{2.5R}$ ($\mu mol\,\mu g^{-1}$)	0.0115 ± 0.0026	0.0105 ± 0.0023	0.0101 ± 0.0017	0.0106 ± 0.0016

[a] $F(SO_4^{2-})$ is the fraction of SO_4^{2-} in $PM_{2.5}$ mass, which was calculated using SO_4^{2-} concentrations divided by $PM_{2.5R}$ concentrations. [b] $F(NO_3^-)$ is the fraction of NO_3^- in $PM_{2.5}$ mass. The calculation method is the same as that for $F(SO_4^{2-})$.

the main contributors to WSIs. During daytime, SO_4^{2-} and NO_3^- were $13.97 \pm 5.19\,\mu g\,m^{-3}$ and $5.82 \pm 3.49\,\mu g\,m^{-3}$, respectively, serving as the major acidic species and accounting for 42.9 % and 15.7 % of the $PM_{2.5}$ mass (Table 1 and Fig. 2). At night, SO_4^{2-} and NO_3^- concentrations decreased slightly, which were $10.97 \pm 8.06\,\mu g\,m^{-3}$ and $5.63 \pm 4.87\,\mu g\,m^{-3}$, respectively, representing 36.8 % and 17.7 % of the $PM_{2.5}$ mass (Table 1 and Fig. 2). In other words, the two main acid species, SO_4^{2-} and NO_3^-, occupied slightly larger fractions of the $PM_{2.5}$ mass during the daytime (58.7 %) compared to the nighttime (54.6 %), along with the lower ALWC, resulting in the lower aerosol pH of 0.46 ± 0.83 during daytime (Table 1). At night, aerosol pH (1.06 ± 0.96) increased by a factor of 2.3 compared to daytime.

The aerosol pH calculated in this work was evidently lower than many other areas of China (Liu et al., 2017; Wang et al., 2019; Xu et al., 2020). During the clean period, air masses mainly originated from the seas. Therefore, the aerosol pH can be very acidic because of the lack of sources of alkaline substances over the ocean, such as NH_3, Ca^{2+}, et al. (Zhou et al., 2018). Compared to the inland areas, much lower aerosol pH in coastal areas is reasonable (Wang et al., 2022). For instance, Zhou et al. (2018) reported that the pH of aerosols near the Bohai Sea can be as low as around 1.0. Moreover, they also found that the daytime aerosol acidity was significantly stronger than that during the nighttime in coastal areas. This observation aligns with the findings during clean periods in our study, which were characterized by the predominance of sea breezes. In this study, we employed the ratio of acidic substances to PM, namely, $(2[SO_4^{2-}] + [NO_3^-])/PM_{2.5R}$, to characterize the level of acidic substances in a unit of $PM_{2.5}$ because SO_4^{2-} and NO_3^- were predominant acidic species within WSIs (> 75 % in mass). It was $0.0115 \pm 0.0026\,\mu mol\,\mu g^{-1}$ and $0.0105 \pm 0.0023\,\mu mol\,\mu g^{-1}$ in $PM_{2.5}$ mass during daytime and nighttime, respectively (Table 1).

During the SP period, WSIs retained similar proportions in $PM_{2.5}$ as during the clean period, accounting for 70.5 % and 74.3 % during daytime and nighttime, respectively. SO_4^{2-}, NO_3^-, and NH_4^+ were also the main contributors to WSIs. In the daytime, the concentrations of SO_4^{2-} and NO_3^- were $14.94 \pm 5.81\,\mu g\,m^{-3}$ and $26.71 \pm 13.15\,\mu g\,m^{-3}$, respectively, showing a marginal elevation over nighttime levels (Table 1). However, SO_4^{2-} had evidently lower contributions to $PM_{2.5}$ compared to the clean period, which were only 20.9 % and 23.0 % during daytime and nighttime, respectively (Table 1 and Fig. 2). In contrast, NO_3^- had a noticeably higher contribution to $PM_{2.5}$ compared to the clean period, exhibiting little diurnal variation, with percentages of 35.4 % and 35.6 % during daytime and nighttime, respectively (Table 1 and Fig. 2). In total, the ratio of acids to PM (i.e., $(2[SO_4^{2-}]+[NO_3^-])/PM_{2.5R}$) was $0.0101 \pm 0.0017\,\mu mol\,\mu g^{-1}$ during daytime and $0.0106 \pm 0.0016\,\mu mol\,\mu g^{-1}$ during nighttime (Table 1). Even though the ALWC ($44.1 \pm 33.8\,\mu g\,m^{-3}$) was significantly more abundant at night compared to the daytime ($22.5 \pm 13.2\,\mu g\,m^{-3}$), the aerosol pH was lower at night. Specifically, the nighttime aerosol pH was 0.98 ± 0.75, while the daytime aerosol pH was slightly higher at 1.16 ± 0.88, indicating weaker aerosol acidity during daytime with a 18.4 % increase in pH compared to nighttime aerosols.

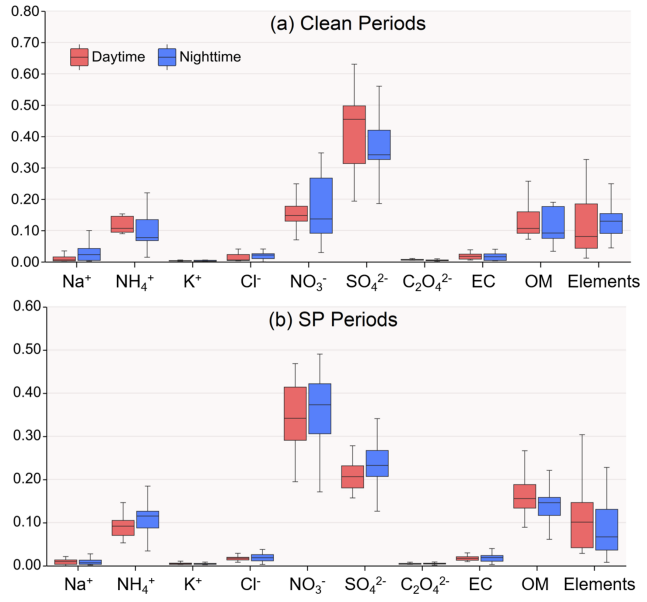

Figure 2. Mass fractions of chemical species in reconstructed $PM_{2.5}$ mass during daytime and nighttime in clean and SP conditions. Mg^{2+} and Ca^{2+} are not shown in the above pictures because total Mg is included in elements data and total Ca is assessed by 0.8 times Al.

4 Discussion

We found that daytime $\%Fe_S$ was much higher than nighttime $\%Fe_S$ during the clean period, while the opposite pattern emerged during the SP period. This section delves into the primary factors driving the distinct diurnal shifts in aerosol $\%Fe_S$ during clean and SP periods based on the aspects of aqueous-phase conversions and photocatalysis reactions.

4.1 Aqueous-phase conversions promoted by acid processes

The $\%Fe_S$ was dependent on the acidification of the aerosol particles, and high $\%Fe_S$ was associated with low aerosol pH (Table 1). The pH of aerosols is controlled by ALWC and H^+ contents. The predominant acidic species, i.e., SO_4^{2-} and NO_3^-, play crucial roles in promoting the dissolution of insoluble Fe through proton-promoted reactions. As shown in Fig. 3a, there was a significant negative correlation between the aerosol pH and the relative content of these two acidic species when the pH was below 4. Especially during clean and SP periods ($r = 0.62$, Fig. 3a), the slope of the regression line was approximately -602.99, indicating that a variation of $1.0\,nmol\mu g^{-1}$ of the acidic species content in $PM_{2.5}$ can lead to a noticeable fluctuation in aerosol pH (about 0.60). For instance, the daytime aerosol pH was 0.60 lower than that of the nighttime during the clean period, even though the difference of the two acidic species content was only about $1.0\,nmol\,\mu g^{-1}$.

There was no prominent correlation between pH and ALWC when the pH exceeded 6 (Fig. 3b). When the pH was smaller than 6, the increasing ALWC facilitated the heterogeneous reactions of SO_2 and NO_2 to generate more SO_4^{2-} and NO_3^-, lowering the aerosol pH and enhancing the $\%Fe_S$. The formation of SO_4^{2-} and NO_3^- will further facilitate the growth of ALWC due to their remarkable hygroscopicity, establishing a positive feedback (Path A in Fig. 4), referred to as the "ALWC-acid" feedback (Wang et al., 2016; Wu et al., 2018b). On the other hand, ALWC dilutes H^+ in aerosol water. This process weakens the aerosol acidity and inhibits the particles from $\%Fe_S$ elevation (Path B in Fig. 4). In addition, the increasing ALWC served as a medium for loading water-soluble components may promote the formation of Fe_S (Path C in Fig. 4). The profound influence of acidic species on the aerosol pH indicates the predominance of the "ALWC-acid" feedback in modulating the aerosol pH and augmenting $\%Fe_S$ (Figs. 3a, 3c and S4). The high $\%Fe_S$ we observed during daytime and nighttime can be attributed to the relatively high content of acidic species in $PM_{2.5}$.

RH is a key factor in the formation of SO_4^{2-} and NO_3^- through heterogeneous/aqueous-phase reactions within aerosols (Wang et al., 2016; Liu et al., 2020; Hou et al., 2022). As demonstrated in Fig. 5, the strong dependency of the oxidation rate of sulfur (SOR, defined as $[SO_4^{2-}]/([SO_4^{2-}]+[SO_2])$ on RH was observed under moderate humid conditions ($r = 0.64$, $p < 0.01$). However, the oxidation rate of nitrogen (NOR, defined as $[NO_3^-]/([NO_3^-]+[NO_2])$ had a poor dependence on RH ($r = 0.46$, $p > 0.05$). A decrease of 10 % in RH resulted in a notable reduction of 7.6 % in SOR (Fig. 5). Such a striking RH dependence was observed mainly during the SP period, indicating the significant role of heterogeneous reactions in controlling the formation of SO_4^{2-}. Therefore, the facilitation of aqueous-phase conversions leading to the formation of SO_4^{2-} was more pronounced at night during the SP period, attributed to the high RH. This, in turn, resulted in a high proportion of SO_4^{2-} and acidic species, as well as the elevated SOR (Table 1, Figs. 2b and S5). The nighttime aerosol pH was approximately 0.18 units lower than that during daytime, but this slight variation did not hinder the efficient formation of Fe_S during nighttime in SP periods.

In contrast, RH was generally above 80 % during daytime and nighttime in clean periods. The SOR was 0.49 on average and did not exhibit a clear correlation with RH beyond 78 % (Fig. 5a). Similar phenomena have been observed in previous studies, suggesting the existence of a saturation point in the promotion of RH on the aqueous-phase formation of SO_4^{2-} (Wang et al., 2019, 2021). High RH (> 70 %) can cause water-soluble species to deliquesce and form an aqueous layer on the particle surface. Once the aqueous layer forms, the influence of RH variations becomes minimal (Shi et al., 2022). Hence, the degree of aqueous-phase processes

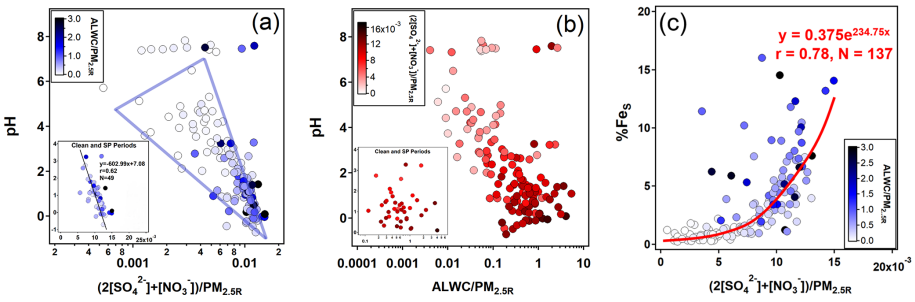

Figure 3. Relationships among pH, the normalized relative abundance of ALWC (unit: $\mu g\,m^{-3}$), and main acidic species ($= 2[SO_4^{2-}] + [NO_3^-]$, unit: $\mu mol\,m^{-3}$) with respect to the reconstructed $PM_{2.5}$ (i.e., $PM_{2.5R}$, unit: $\mu g\,m^{-3}$) and $\%Fe_S$. The subgraph at the bottom-left of panels **(a)** and **(b)** shows scatter plots during clean and SP periods with the linear regression line obtained using the Igor Pro-based program developed by Wu and Yu (2018).

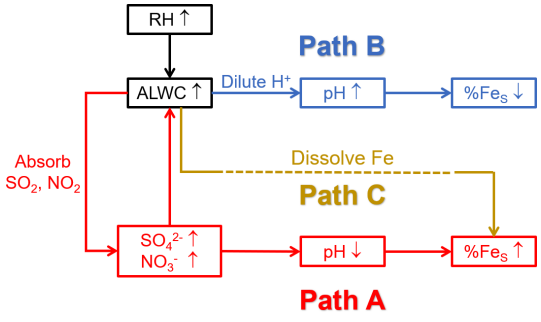

Figure 4. Schematic diagram of ALWC affecting pH and $\%Fe_S$. Path C is challenging to observe and quantify because of the Fe_S extraction using Milli-Q water in the sample pretreatment.

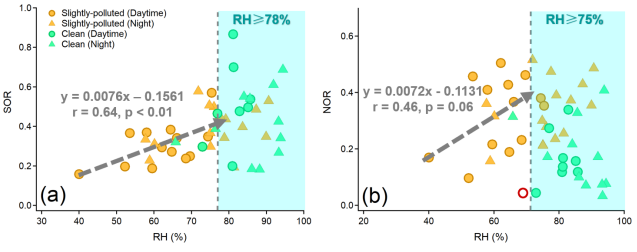

Figure 5. The dependence of SOR **(a)** and NOR **(b)** on RH during clean and slightly polluted periods. The fitting of the regression line between SOR and RH was fitted when RH < 78 %. The fitting of the regression line between NOR and RH was fitted when RH < 75 % and one deviation point (the red circle in **(b)**) was removed.

promoting SO_4^{2-} formation during clean periods was similar across both daytime and nighttime.

4.2 Daytime enhancement by photocatalysis reactions

4.2.1 The influence of photochemical processes on sulfate formation

Photochemical reactions can enhance the formation of acidic species and increase the aerosol $\%Fe_S$ through aerosol acidification (Tao et al., 2020; L. Liu et al., 2021). The large proportion of acidic species during the daytime of the clean period was attributable to SO_4^{2-}, which was 6.1 % higher than the nighttime SO_4^{2-} (Table 1 and Fig. 2a). Despite similar levels of SO_2 observed during daytime and nighttime, the daytime SOR reached as high as 0.50 ± 0.20 (Fig. S5). The conversion rates in the aqueous phase were similar during daytime and nighttime in clean periods. Therefore, the substantial fraction of SO_4^{2-} was most likely caused by photochemical reactions.

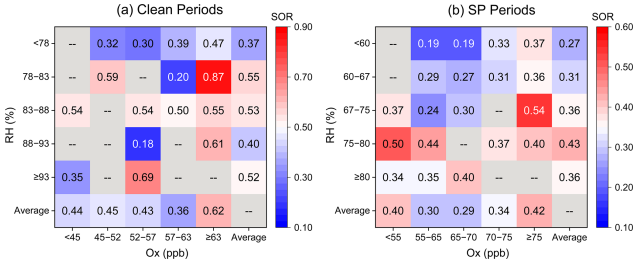

Figure 6. RH–O_X image plots colored by SOR during clean and SP periods. The last rows and columns of the matrices represent the average value of SOR in the corresponding ranges of RH and O_X.

O_x (described by the sum of O_3 and NO_2) was investigated to quantify the potential of photochemical reactions, following the method of Wu et al. (2018a). The daytime O_x concentration (56.1 ± 6.4 ppb) was about 5.1 % higher than that of nighttime O_x (53.4 ± 9.3 ppb) during the clean period. The substantial SOR occurred under the extreme O_x conditions (Fig. 6a), suggesting a significant contribution of the photochemical reactions during the clean period. The enhancement of daytime photochemistry and aqueous chemistry on aerosol $\%Fe_S$ was more pronounced than that of the nighttime aqueous reactions solely during the clean period (Fig. 7a and b).

During the SP period, the extent of SOR was more influenced by RH than by O_x, especially when RH was below 80 % (Fig. 6b). Nighttime SOR (0.37 ± 0.12) was approximately 1.2 times higher than the daytime SOR (0.31 ± 0.11)

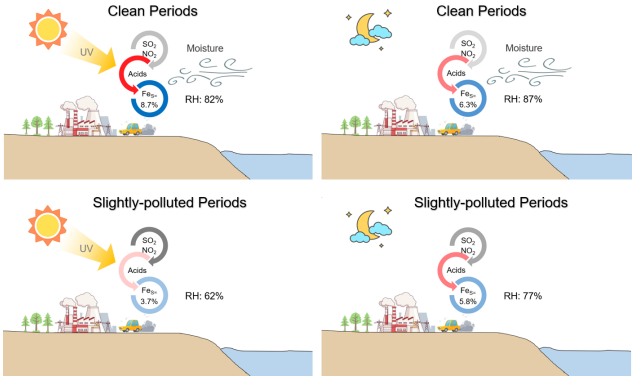

Figure 7. Conceptual diagram showing the Fe dissolution influenced by acid processes at the coastal city during daytime and nighttime in clean and SP periods.

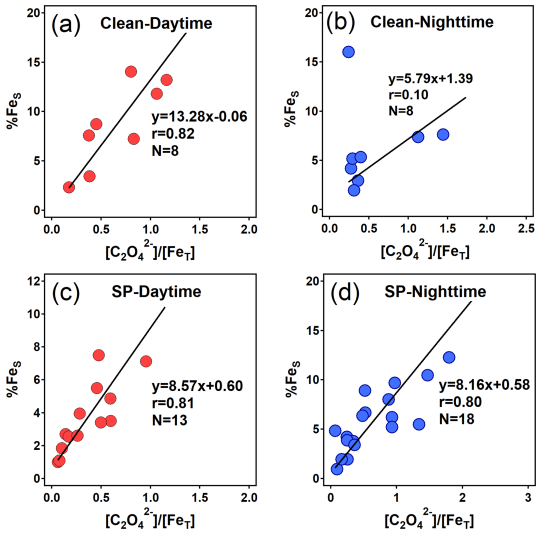

Figure 8. Relationships between $\%Fe_S$ and the molar ratio (unit: $\mu mol\,\mu mol^{-1}$) of oxalate to Fe_T during daytime and nighttime in clean and SP periods. An extreme point ($\%Fe_S = 37.2\,\%$) in **(b)** was removed.

even though the daytime O_x was higher than that during nighttime (Fig. S5), indicating a greater contribution of liquid/heterogeneous reactions to the SO_4^{2-} formation than photocatalytic reactions. Similar findings were reported by Hou et al. (2022), who highlighted the dominant role of humidity rather than O_x in SO_4^{2-} formation in haze intensification. The nighttime exhibited a more significant "ALWC-acid" feedback compared to the daytime during the SP period. The influence of daytime photochemistry combined with aqueous-phase reactions was comparatively weaker than nighttime aqueous chemistry, leading to the higher $\%Fe_S$ at night (Fig. 7c and d). Notably, O_x concentrations were significantly higher during the SP period in comparison to the clean period (Fig. S5), indicating more active daytime photocatalytic reactions. However, the impact of aqueous-phase conversions during the SP nighttime period was relatively weak compared to the nighttime of the clean period. These results suggest that the role of photocatalytic reactions in SO_4^{2-} formation, and subsequently in the elevation of aerosol $\%Fe_S$, was feeble compared to aqueous-phase conversions.

Enhancing aerosol $\%Fe_S$ through direct photocatalysis pathways is indeed possible. Iron oxides in minerals can generate conduction band electrons upon irradiation, causing the reductive dissolution of Fe(III)-containing solid phases to Fe(II) species (Zhang et al., 1993; Fu et al., 2010). However, structural Fe(III), which is the major iron-related mineral in dust and coal fly ash, does not readily undergo direct reduction upon UV irradiation (Fu et al., 2012, 2010; Xie et al., 2020). Another pathway for photolysis-induced iron dissolution involves the reduction by reactive oxygen species (ROS, e.g., $O_2^{\bullet-}$, $HO_2^{\bullet}$, and H_2O_2). These ROS can be generated from dissolved oxygen accompanied by conduction band electrons, enhancing the Fe dissolution by reducing the solid-phase Fe(III) into the more soluble Fe(II) form (Zhu et al., 1997; Hettiarachchi and Rubasinghege, 2020). Aerosol water is necessary for the above reactions, and the proton-promoted dissolution by acid species is indispensable to dissolve the solid-phase Fe(II) into aerosol solutions. We suppose that the observed weak influence of photocatalysis on $\%Fe_S$ was because of the extreme aerosol acidity. The acidity of aerosols, such as a pH as low as 2.0 during daytime of the present study, can suppress the contribution of photochemical catalysis in the formation of Fe_S (Zhu et al., 1993; Fu et al., 2010, 2012). In addition, studies have suggested that Fe dissolution can be inhibited in H_2SO_4 systems under irradiation compared to dark conditions, which could be another reason for the low $\%Fe_S$ during daytime, although the exact mechanism remains unclear (Fu et al., 2010; Hettiarachchi et al., 2018).

4.2.2 The enhancement of $\%Fe_S$ promoted by oxalate-related conversions

Oxalate can form complexes with Fe(III) and participate in photochemical reactions through photoinduced charge transfer. Oxalate transfers its charge to the Fe(III) surface via photolytic reactions during daytime, resulting in the reduction of Fe(III) to Fe(II), followed by the dissociation of the formed Fe(II) from the surface and hence the dissolution of aerosol Fe (Zuo and Hoigne, 1992; Zhang et al., 2019; Lueder et al., 2020). Shi et al. (2022) identified the oxalate/Fe_T ratio as an excellent predictor for aerosol $\%Fe_S$ through machine learning, underscoring its remarkable effectiveness. However, field observations rarely confirm its influence on Fe_S from the perspective of oxalate-Fe photochemistry.

In this study, significant correlations were observed between $\%Fe_S$ and the molar ratio of [oxalate]/[Fe_T] during daytime in both clean periods ($r = 0.82$) and SP periods ($r = 0.81$) (Fig. 8a and c). Similarly, a striking correlation was

also found in nighttime during the SP period ($r = 0.80$), albeit with a lower slope of 8.16 in the regression line (Fig. 8d). Noteworthy is the strong dependence of $\%Fe_S$ (or Fe_S) on oxalate concentration at night (Figs. 8d, S6b and S6d). Field observations highlight the pivotal role of organic compound complexation in stabilizing Fe (Sakata et al., 2022). Additionally, as illustrated by Fig. 8a and c, the variation in $\%Fe_S$ induced by each unit variation in daytime [oxalate]/[Fe_T] was greater than its nighttime equivalent. The most notable increase was observed during the clean period, with a daytime slope of 13.28, marking a 1.5-fold increase over the SP period (daytime slope = 8.57). Similarly, the concentration of Fe_S per unit of oxalate showed a parallel trend, marking the highest daytime slope of the clean period during the campaign (Fig. S6). Such patterns imply that enhanced sunlight in clean days may have catalyzed photochemical processes involving daytime oxalate-Fe, leading to elevated Fe_S and $\%Fe_S$. While these outcomes have only been discussed through laboratory simulations (Chen and Grassian, 2013) or indirectly by examining oxalate degradation or sulfate formation (Zhou et al., 2020), they have now been empirically discovered through field observations in this study.

Simultaneously, Fe_S species redox reactions can facilitate the formation of oxalate in return if the precursors are abundant, particularly with aqueous-phase reactions playing a pivotal role when RH exceeds 60 % (Zhang et al., 2019). This may elucidate one of the main reasons behind the significant correlations observed between Fe_S and oxalate. Notably, oxalate concentration was higher during the daytime compared to the nighttime in this study (Fig. S5), concomitant with elevated Fe_S concentrations. The photocatalytic degradation of oxalate-Fe, promoting Fe dissolution during daytime, was unlikely to be the predominant pathway influencing the oxalate concentration, otherwise a decrease in oxalate concentration would occur (Dou et al., 2021). Therefore, the oxalate formation process catalyzed by Fe_S could yield a higher production rate of oxalate during the daytime than at night. Figure S7 portrays the conceptual diagram of these conversion processes. Similar scenarios might unfold for SO_4^{2-} formation due to the heightened Fe redox reactions during daytime (Zhou et al., 2020). Owing to the extremely low aerosol pH (< 2), pathways catalyzed by transition-metal ions (TMIs, e.g., Fe_S) could primarily influence the secondary formation of SO_4^{2-}, leading to potent aerosol acidity (T. Liu et al., 2021). The elevated aerosol acidity, in turn, fostered the formation of Fe_S, thus furthering the generation of SO_4^{2-} and oxalate under high RH conditions. The resulting oxalate could then be complexed with Fe_S, sustaining $\%Fe_S$ at a high level at night.

To summarize, the findings of this study suggest that daytime photochemical processes indeed facilitated the dissolution of aerosol Fe, consequently elevating $\%Fe_S$ during the clean period. This mechanism, in turn, may foster the secondary formation of oxalate and SO_4^{2-}. The complexation of organic compounds significantly contributed to maintaining the high $\%Fe_S$ at night. During SP periods, the diurnal variation in aerosol $\%Fe_S$ mainly resulted from the differing levels of aerosol acidity between daytime and nighttime rather than oxalate-related conversions, a conclusion strongly supported by the higher $\%Fe_S$ observed at night compared to daytime (Fig. 8c and d).

4.3 Environmental implications

Limited research has explored the diurnal variation of aerosol $\%Fe_S$. Only an early case investigated the diel variability of Fe species at an island located in the Caribbean Sea and highlighted the photochemical processing of Fe (Zhu et al., 1997). This study found a pronounced correlation between Fe_S and acid species within an aerosol pH range of 0 to 1, emphasizing the considerable influence of aerosol acidification on Fe dissolution. These findings align with the results of our study. Our results suggest that acid-driven aqueous-phase transformations could have a more crucial role in altering aerosol $\%Fe_S$ than photochemical reactions under certain conditions in coastal urban areas.

Previous studies pinpointed robust $\%Fe_S$ of anthropogenic aerosols, especially for combustion-related fly ash (Oakes et al., 2012; Wang et al., 2015; Baldo et al., 2022; Li et al., 2022). Unlike urban air, RH tends to be considerably higher over open oceans, fostering an environment where heterogeneous reactions and the secondary formation of SO_4^{2-} and NO_3^- are prevalent. In such cases, photochemical reactions and precursor concentrations will determine the formation of salts. Given that the air mass of the clean period comprised a mix of marine and local urban air, it is expected that the Fe dissolution in aerosol particles is an effective way to produce Fe_S during daylight hours. Air masses moving from densely populated land areas carry substantial amounts of SO_2, NO_2, and NH_3 to offshore areas, aiding in the formation of SO_4^{2-} and NO_3^- and conducing to the acidic dissolution of Fe in aerosol particles. Subsequently, the solubilized Fe, through proton-promoted dissolution, can be further stabilized by the organic complexation of Fe in the marine atmosphere, as indicated by Sakata et al. (2022).

Additionally, on the one hand the dearth of ammonia sources in the marine atmosphere may hinder the formation of SO_4^{2-} and NO_3^- to some extent (Wang et al., 2017; Guo et al., 2018). On the other hand, the limited availability of ammonia may be also conducive to enhancing the aerosol acidity and elevating aerosol $\%Fe_S$. Considering that concentrations of HCl in remote marine atmospheric boundary layer are typically higher than in the continent of East Asia, the influence of chloride on aerosol pH may therefore play a conspicuous role in regulating $\%Fe_S$ (Tobo et al., 2010), of which knowledge is very limited.

5 Summary

This study investigated the daytime and nighttime $\%Fe_S$ in $PM_{2.5}$ in a coastal city of China under clean and SP conditions. Under clean conditions, $\%Fe_S$ was higher during daytime (8.7 %) compared to the nighttime (6.3 %, after removing an extreme point of 37.2 %). On the contrary, under SP conditions $\%Fe_S$ was higher at night (5.8 %) than during daytime (3.7 %). Significant correlations were observed between the main acidic components (SO_4^{2-} and NO_3^-), aerosol pH, and $\%Fe_S$, indicating that the acid process played a dominant role in influencing aerosol $\%Fe_S$.

The RH consistently exceeded 80 % during both daytime and nighttime in clean periods. Aqueous-phase reactions were found to be most effective in promoting the secondary formation of acid species, with photochemical processes further enhancing SO_4^{2-} formation during daytime. Together with the lower ALWC, the aerosol pH was much lower during daytime (0.46 ± 0.83) compared to nighttime (1.06 ± 0.96) during the clean period, which exerted a more significant influence on aerosol Fe dissolution. In contrast, RH was much higher at night (76.8 %) than that during daytime (62.1 %) in the SP period. The dry conditions during daytime notably restricted the secondary formation of SO_4^{2-} and NO_3^-. The acid content in $PM_{2.5}$ was much higher at night under the promotion of heterogeneous processes, resulting in stronger aerosol acidity and higher aerosol $\%Fe_S$. Furthermore, photochemical reactions associated with oxalate likely played a considerable role in enhancing $\%Fe_S$ during daylight hours, a trend that is more noticeable during the clean period. Oxalate might also be crucial in sustaining elevated $\%Fe_S$ at night during the SP period.

This study provides insights into the mechanisms of aerosol $\%Fe_S$ modulation in the coastal city. The robust promotion of aqueous-phase processes and the comparatively weaker influence of photochemistry on enhancing aerosol $\%Fe_S$ were observed. In urban air, RH was a crucial factor in controlling $\%Fe_S$ through modulating the heterogeneous reactions of SO_4^{2-} and NO_3^-. In contrast, in the oceanic atmospheric boundary layer, precursor levels and photochemical processes may be the decisive manipulators of aerosol $\%Fe_S$. Therefore, the content of bioavailable Fe in urban-related aerosols may be greatly elevated after intrusion into the marine atmosphere, which holds significant importance for future research.

Code and data availability. The software code and data sets used in this study are available from the corresponding author upon request (yangzhou@ouc.edu.cn).

Supplement. The supplement related to this article is available online at: https://doi.org/10.5194/acp-24-6495-2024-supplement.

Author contributions. WL: investigation, formal analysis, writing – original draft, writing – review and editing. YQ: methodology. YL: methodology. GW: visualization. YZ: methodology. JS: methodology. WQ: methodology. LS: supervision, funding acquisition. WW: methodology. DZ: funding acquisition, methodology, writing – review and editing. YZ: conceptualization, funding acquisition, methodology, supervision, writing – review and editing.

Competing interests. The contact author has declared that none of the authors has any competing interests.

Disclaimer. Publisher's note: Copernicus Publications remains neutral with regard to jurisdictional claims made in the text, published maps, institutional affiliations, or any other geographical representation in this paper. While Copernicus Publications makes every effort to include appropriate place names, the final responsibility lies with the authors.

Special issue statement. This article is part of the special issue "RUSTED: Reducing Uncertainty in Soluble aerosol Trace Element Deposition (AMT/ACP/AR/BG inter-journal SI)". It is not associated with a conference.

Acknowledgements. We gratefully acknowledge the National Oceanic and Atmospheric Administration (NOAA) Air Resources Laboratory (ARL) for the provision of the HYSPLIT transport and dispersion model, available at (https://www.ready.noaa.gov/HYSPLIT.php, last access: 15 April 2024), and the Global Data Assimilation System (GDAS). Additionally, we acknowledge the use of ISORROPIA II, accessible at (https://www.epfl.ch/labs/lapi/models-and-software/isorropia/, last access: 17 April 2024), developed by the Schools of Earth & Atmospheric Sciences and Chemical & Biomolecular Engineering at the Georgia Institute of Technology, for the calculation of aerosol pH and liquid water content.

Financial support. This research has been supported by the National Natural Science Foundation of China (grant nos. 41875155, 41605114, and 41875174) and the Japan Society for the Promotion of Science (grant no. 21H01158).

Review statement. This paper was edited by James Allan and reviewed by Weijun Li and one anonymous referee.

References

Arimoto, R., Zhang, X. Y., Huebert, B. J., Kang, C. H., Savoie, D. L., Prospero, J. M., Sage, S. K., Schloesslin, C. A., Khaing, H. M., and Oh, S. N.: Chemical composition of atmospheric aerosols from Zhenbeitai, China, and Gosan, South Korea, during ACE-Asia, J. Geophys. Res.-Atmos., 109, D19S04, https://doi.org/10.1029/2003JD004323, 2004.

Baldo, C., Ito, A., Krom, M. D., Li, W., Jones, T., Drake, N., Ignatyev, K., Davidson, N., and Shi, Z.: Iron from coal combustion particles dissolves much faster than mineral dust under simulated atmospheric acidic conditions, Atmos. Chem. Phys., 22, 6045–6066, https://doi.org/10.5194/acp-22-6045-2022, 2022.

Chen, H. and Grassian, V. H.: Iron Dissolution of Dust Source Materials during Simulated Acidic Processing: The Effect of Sulfuric, Acetic, and Oxalic Acids, Environ. Sci. Technol., 47, 10312–10321, https://doi.org/10.1021/es401285s, 2013.

Chen, Y. and Siefert, R. L.: Seasonal and spatial distributions and dry deposition fluxes of atmospheric total and labile iron over the tropical and subtropical North Atlantic Ocean, J. Geophys. Res.-Atmos., 109, D09305, https://doi.org/10.1029/2003JD003958, 2004.

Dou, J., Alpert, P. A., Corral Arroyo, P., Luo, B., Schneider, F., Xto, J., Huthwelker, T., Borca, C. N., Henzler, K. D., Raabe, J., Watts, B., Herrmann, H., Peter, T., Ammann, M., and Krieger, U. K.: Photochemical degradation of iron(III) citrate/citric acid aerosol quantified with the combination of three complementary experimental techniques and a kinetic process model, Atmos. Chem. Phys., 21, 315–338, https://doi.org/10.5194/acp-21-315-2021, 2021.

Fu, H., Cwiertny, D. M., Carmichael, G. R., Scherer, M. M., and Grassian, V. H.: Photoreductive dissolution of Fe-containing mineral dust particles in acidic media, J. Geophys. Res.-Atmos., 115, D11304, https://doi.org/10.1029/2009JD012702, 2010.

Fu, H., Lin, J., Shang, G., Dong, W., Grassian, V. H., Carmichael, G. R., Li, Y., and Chen, J.: Solubility of Iron from Combustion Source Particles in Acidic Media Linked to Iron Speciation, Environ. Sci. Technol., 46, 11119–11127, https://doi.org/10.1021/es302558m, 2012.

Guo, H., Xu, L., Bougiatioti, A., Cerully, K. M., Capps, S. L., Hite Jr., J. R., Carlton, A. G., Lee, S.-H., Bergin, M. H., Ng, N. L., Nenes, A., and Weber, R. J.: Fine-particle water and pH in the southeastern United States, Atmos. Chem. Phys., 15, 5211–5228, https://doi.org/10.5194/acp-15-5211-2015, 2015.

Guo, H., Otjes, R., Schlag, P., Kiendler-Scharr, A., Nenes, A., and Weber, R. J.: Effectiveness of ammonia reduction on control of fine particle nitrate, Atmos. Chem. Phys., 18, 12241–12256, https://doi.org/10.5194/acp-18-12241-2018, 2018.

Hennigan, C. J., Izumi, J., Sullivan, A. P., Weber, R. J., and Nenes, A.: A critical evaluation of proxy methods used to estimate the acidity of atmospheric particles, Atmos. Chem. Phys., 15, 2775–2790, https://doi.org/10.5194/acp-15-2775-2015, 2015.

Hettiarachchi, E. and Rubasinghege, G.: Mechanistic Study on Iron Solubility in Atmospheric Mineral Dust Aerosol: Roles of Titanium, Dissolved Oxygen, and Solar Flux in Solutions Containing Different Acid Anions, ACS Earth Space Chem., 4, 101–111, https://doi.org/10.1021/acsearthspacechem.9b00280, 2020.

Hettiarachchi, E., Hurab, O., and Rubasinghege, G.: Atmospheric Processing and Iron Mobilization of Ilmenite: Iron-Containing Ternary Oxide in Mineral Dust Aerosol, The J. Phys. Chem. A, 122, 1291–1302, https://doi.org/10.1021/acs.jpca.7b11320, 2018.

Hettiarachchi, E., Reynolds, R. L., Goldstein, H. L., Moskowitz, B., and Rubasinghege, G.: Bioavailable iron production in airborne mineral dust: Controls by chemical composition and solar flux, Atmos. Environ., 205, 90–102, https://doi.org/10.1016/j.atmosenv.2019.02.037, 2019.

Hou, L., Dai, Q., Song, C., Liu, B., Guo, F., Dai, T., Li, L., Liu, B., Bi, X., Zhang, Y., and Feng, Y.: Revealing Drivers of Haze Pollution by Explainable Machine Learning, Environ. Sci. Technol. Lett., 9, 112–119, https://doi.org/10.1021/acs.estlett.1c00865, 2022.

Huang, K., Zhuang, G., Li, J., Wang, Q., Sun, Y., Lin, Y., and Fu, J. S.: Mixing of Asian dust with pollution aerosol and the transformation of aerosol components during the dust storm over China in spring 2007, J. Geophys. Res.-Atmos., 115, D00K13, https://doi.org/10.1029/2009JD013145, 2010.

Li, J., Zhang, Y.-L., Cao, F., Zhang, W., Fan, M., Lee, X., and Michalski, G.: Stable Sulfur Isotopes Revealed a Major Role of Transition-Metal Ion-Catalyzed SO_2 Oxidation in Haze Episodes, Environ. Sci. Technol., 54, 2626–2634, https://doi.org/10.1021/acs.est.9b07150, 2020.

Li, K., Fang, X., Wang, T., Gong, K., Ali Tahir, M., Wang, W., Han, J., Cheng, H., Xu, G., and Zhang, L.: Atmospheric organic complexation enhanced sulfate formation and iron dissolution on nano α-Fe_2O_3, Environ. Sci. Nano, 8, 698–710, https://doi.org/10.1039/D0EN01220C, 2021.

Li, R., Zhang, H., Wang, F., He, Y., Huang, C., Luo, L., Dong, S., Jia, X., and Tang, M.: Mass fractions, solubility, speciation and isotopic compositions of iron in coal and municipal waste fly ash, Sci. Total Environ., 838, 155974, https://doi.org/10.1016/j.scitotenv.2022.155974, 2022.

Li, W., Xu, L., Liu, X., Zhang, J., Lin, Y., Yao, X., Gao, H., Zhang, D., Chen, J., Wang, W., Harrison, R. M., Zhang, X., Shao, L., Fu, P., Nenes, A., and Shi, Z.: Air pollution–aerosol interactions produce more bioavailable iron for ocean ecosystems, Sci. Adv., 3, e1601749, https://doi.org/10.1126/sciadv.1601749, 2017.

Li, W., Qi, Y., Qu, W., Qu, W., Shi, J., Zhang, D., Liu, Y., Zhang, Y., Zhang, W., Ren, D., Ma, Y., Wang, X., Yi, L., Sheng, L., and Zhou, Y.: $PM_{2.5}$ source apportionment identified with total and soluble elements in positive matrix factorization, Sci. Total Environ., 858, 159948, https://doi.org/10.1016/j.scitotenv.2022.159948, 2023a.

Li, W., Qi, Y., Qu, W., Qu, W., Shi, J., Zhang, D., Liu, Y., Wu, F., Ma, Y., Zhang, Y., Ren, D., Du, X., Yang, S., Wang, X., Yi, L., Gao, X., Wang, W., Ma, Y., Sheng, L., and Zhou, Y.: Sulfate and nitrate elevation in reverse-transport dust plumes over coastal areas of China, Atmos. Environ., 295, 119518, https://doi.org/10.1016/j.atmosenv.2022.119518, 2023b.

Liu, L., Lin, Q., Liang, Z., Du, R., Zhang, G., Zhu, Y., Qi, B., Zhou, S., and Li, W.: Variations in concentration and solubility of iron in atmospheric fine particles during the COVID-19 pandemic: An example from China, Gondwana Res., 97, 138–144, https://doi.org/10.1016/j.gr.2021.05.022, 2021.

Liu, M., Song, Y., Zhou, T., Xu, Z., Yan, C., Zheng, M., Wu, Z., Hu, M., Wu, Y., and Zhu, T.: Fine particle pH during severe haze episodes in northern China, Geophys. Res. Lett., 44, 5213–5221, https://doi.org/10.1002/2017GL073210, 2017.

Liu, P., Ye, C., Xue, C., Zhang, C., Mu, Y., and Sun, X.: Formation mechanisms of atmospheric nitrate and sulfate during the winter haze pollution periods in Beijing: gas-phase, heterogeneous and aqueous-phase chemistry, Atmos. Chem. Phys., 20, 4153–4165, https://doi.org/10.5194/acp-20-4153-2020, 2020.

Liu, T., Chan, A. W. H., and Abbatt, J. P. D.: Multiphase Oxidation of Sulfur Dioxide in Aerosol Particles: Implications for Sulfate

Formation in Polluted Environments, Environ. Sci. Technol., 55, 4227–4242, https://doi.org/10.1021/acs.est.0c06496, 2021.

Lueder, U., Jørgensen, B. B., Kappler, A., and Schmidt, C.: Photochemistry of iron in aquatic environments, Environ. Sci.-Proc. Imp., 22, 12–24, https://doi.org/10.1039/C9EM00415G, 2020.

Martin, J. H., Coale, K. H., Johnson, K. S., Fitzwater, S. E., Gordon, R. M., Tanner, S. J., Hunter, C. N., Elrod, V. A., Nowicki, J. L., Coley, T. L., Barber, R. T., Lindley, S., Watson, A. J., Van Scoy, K., Law, C. S., Liddicoat, M. I., Ling, R., Stanton, T., Stockel, J., Collins, C., Anderson, A., Bidigare, R., Ondrusek, M., Latasa, M., Millero, F. J., Lee, K., Yao, W., Zhang, J. Z., Friederich, G., Sakamoto, C., Chavez, F., Buck, K., Kolber, Z., Greene, R., Falkowski, P., Chisholm, S. W., Hoge, F., Swift, R., Yungel, J., Turner, S., Nightingale, P., Hatton, A., Liss, P., and Tindale, N. W.: Testing the iron hypothesis in ecosystems of the equatorial Pacific Ocean, Nature, 371, 123–129, https://doi.org/10.1038/371123a0, 1994.

Oakes, M., Ingall, E. D., Lai, B., Shafer, M. M., Hays, M. D., Liu, Z. G., Russell, A. G., and Weber, R. J.: Iron Solubility Related to Particle Sulfur Content in Source Emission and Ambient Fine Particles, Environ. Sci. Technol., 46, 6637–6644, https://doi.org/10.1021/es300701c, 2012.

Pang, H., Zhang, Q., Wang, H., Cai, D., Ma, Y., Li, L., Li, K., Lu, X., Chen, H., Yang, X., and Chen, J.: Photochemical Aging of Guaiacol by Fe(III)–Oxalate Complexes in Atmospheric Aqueous Phase, Environ. Sci. Technol., 53, 127–136, https://doi.org/10.1021/acs.est.8b04507, 2019.

Pye, H. O. T., Nenes, A., Alexander, B., Ault, A. P., Barth, M. C., Clegg, S. L., Collett Jr., J. L., Fahey, K. M., Hennigan, C. J., Herrmann, H., Kanakidou, M., Kelly, J. T., Ku, I.-T., McNeill, V. F., Riemer, N., Schaefer, T., Shi, G., Tilgner, A., Walker, J. T., Wang, T., Weber, R., Xing, J., Zaveri, R. A., and Zuend, A.: The acidity of atmospheric particles and clouds, Atmos. Chem. Phys., 20, 4809–4888, https://doi.org/10.5194/acp-20-4809-2020, 2020.

Sakata, K., Kurisu, M., Takeichi, Y., Sakaguchi, A., Tanimoto, H., Tamenori, Y., Matsuki, A., and Takahashi, Y.: Iron (Fe) speciation in size-fractionated aerosol particles in the Pacific Ocean: The role of organic complexation of Fe with humic-like substances in controlling Fe solubility, Atmos. Chem. Phys., 22, 9461–9482, https://doi.org/10.5194/acp-22-9461-2022, 2022.

Shi, J., Guan, Y., Ito, A., Gao, H., Yao, X., Baker, A. R., and Zhang, D.: High Production of Soluble Iron Promoted by Aerosol Acidification in Fog, Geophys. Res. Lett., 47, e2019GL086124, https://doi.org/10.1029/2019GL086124, 2020.

Shi, J., Guan, Y., Gao, H., Yao, X., Wang, R., and Zhang, D.: Aerosol Iron Solubility Specification in the Global Marine Atmosphere with Machine Learning, Environ. Sci. Technol., 56, 16453–16461, https://doi.org/10.1021/acs.est.2c05266, 2022.

Shi, J.-H., Zhang, J., Gao, H.-W., Tan, S.-C., Yao, X.-H., and Ren, J.-L.: Concentration, solubility and deposition flux of atmospheric particulate nutrients over the Yellow Sea, Deep Sea Res. Part II, 97, 43–50, https://doi.org/10.1016/j.dsr2.2013.05.004, 2013.

Shi, Z., Krom, M. D., Jickells, T. D., Bonneville, S., Carslaw, K. S., Mihalopoulos, N., Baker, A. R., and Benning, L. G.: Impacts on iron solubility in the mineral dust by processes in the source region and the atmosphere: A review, Aeolian Res., 5, 21–42, https://doi.org/10.1016/j.aeolia.2012.03.001, 2012.

Shi, Z. B., Krom, M. D., Bonneville, S., and Benning, L. G.: Atmospheric Processing Outside Clouds Increases Soluble Iron in Mineral Dust, Environ. Sci. Technol., 49, 1472–1477, https://doi.org/10.1021/es504623x, 2015.

Solmon, F., Chuang, P. Y., Meskhidze, N., and Chen, Y.: Acidic processing of mineral dust iron by anthropogenic compounds over the north Pacific Ocean, J. Geophys. Res.-Atmos., 114, D02305, https://doi.org/10.1029/2008JD010417, 2009.

Song, S., Gao, M., Xu, W., Shao, J., Shi, G., Wang, S., Wang, Y., Sun, Y., and McElroy, M. B.: Fine-particle pH for Beijing winter haze as inferred from different thermodynamic equilibrium models, Atmos. Chem. Phys., 18, 7423–7438, https://doi.org/10.5194/acp-18-7423-2018, 2018.

Sorooshian, A., Wang, Z., Coggon, M. M., Jonsson, H. H., and Ervens, B.: Observations of Sharp Oxalate Reductions in Stratocumulus Clouds at Variable Altitudes: Organic Acid and Metal Measurements During the 2011 E-PEACE Campaign, Environ. Sci. Technol., 47, 7747–7756, https://doi.org/10.1021/es4012383, 2013.

Sugie, K., Nishioka, J., Kuma, K., Volkov, Y. N., and Nakatsuka, T.: Availability of particulate Fe to phytoplankton in the Sea of Okhotsk, Mar. Chem., 152, 20–31, https://doi.org/10.1016/j.marchem.2013.03.005, 2013.

Sun, P., Nie, W., Chi, X., Xie, Y., Huang, X., Xu, Z., Qi, X., Xu, Z., Wang, L., Wang, T., Zhang, Q., and Ding, A.: Two years of online measurement of fine particulate nitrate in the western Yangtze River Delta: influences of thermodynamics and N_2O_5 hydrolysis, Atmos. Chem. Phys., 18, 17177–17190, https://doi.org/10.5194/acp-18-17177-2018, 2018.

Tao, W., Su, H., Zheng, G., Wang, J., Wei, C., Liu, L., Ma, N., Li, M., Zhang, Q., Pöschl, U., and Cheng, Y.: Aerosol pH and chemical regimes of sulfate formation in aerosol water during winter haze in the North China Plain, Atmos. Chem. Phys., 20, 11729–11746, https://doi.org/10.5194/acp-20-11729-2020, 2020.

Tobo, Y., Zhang, D., Matsuki, A., and Iwasaka, Y.: Asian dust particles converted into aqueous droplets under remote marine atmospheric conditions, P. Natl. Acad. Sci. USA, 107, 17905, https://doi.org/10.1073/pnas.1008235107, 2010.

Toner, B. M.: An improved model of the ocean iron cycle, Nature, 620, 41–42, https://doi.org/10.1038/d41586-023-02406-x, 2023.

Turpin, B. J. and Lim, H.-J.: Species Contributions to $PM_{2.5}$ Mass Concentrations: Revisiting Common Assumptions for Estimating Organic Mass, Aerosol Sci. Technol., 35, 602–610, https://doi.org/10.1080/02786820119445, 2001.

Wang, G., Tao, Y., Chen, J., Liu, C., Qin, X., Li, H., Yun, L., Zhang, M., Zheng, H., Gui, H., Liu, J., Huo, J., Fu, Q., Deng, C., and Huang, K.: Quantitative Decomposition of Influencing Factors to Aerosol pH Variation over the Coasts of the South China Sea, East China Sea, and Bohai Sea, Environ. Sci. Technol. Lett., 9, 815–821, https://doi.org/10.1021/acs.estlett.2c00527, 2022.

Wang, G., Zhang, R., Gomez, M. E., Yang, L., Zamora, M. L., Hu, M., Lin, Y., Peng, J., Guo, S., Meng, J., Li, J., Cheng, C., Hu, T., Ren, Y., Wang, Y., Gao, J., Cao, J., An, Z., Zhou, W., Li, G., Wang, J., Tian, P., Marrero-Ortiz, W., Secrest, J., Du, Z., Zheng, J., Shang, D., Zeng, L., Shao, M., Wang, W., Huang, Y., Wang, Y., Zhu, Y., Li, Y., Hu, J., Pan, B., Cai, L., Cheng, Y., Ji, Y., Zhang, F., Rosenfeld, D., Liss, P. S., Duce, R. A., Kolb, C. E., and Molina, M. J.: Persistent sulfate formation from Lon-

don Fog to Chinese haze, P. Natl. Acad. Sci. USA, 113, 13630, https://doi.org/10.1073/pnas.1616540113, 2016.

Wang, H., Ding, J., Xu, J., Wen, J., Han, J., Wang, K., Shi, G., Feng, Y., Ivey, C. E., Wang, Y., Nenes, A., Zhao, Q., and Russell, A. G.: Aerosols in an arid environment: The role of aerosol water content, particulate acidity, precursors, and relative humidity on secondary inorganic aerosols, Sci. Total Environ., 646, 564–572, https://doi.org/10.1016/j.scitotenv.2018.07.321, 2019.

Wang, J., Zhao, B., Wang, S., Yang, F., Xing, J., Morawska, L., Ding, A., Kulmala, M., Kerminen, V.-M., Kujansuu, J., Wang, Z., Ding, D., Zhang, X., Wang, H., Tian, M., Petäjä, T., Jiang, J., and Hao, J.: Particulate matter pollution over China and the effects of control policies, Sci. Total Environ., 584–585, 426–447, https://doi.org/10.1016/j.scitotenv.2017.01.027, 2017.

Wang, Q., Zhuang, G., Li, J., Huang, K., Zhang, R., Jiang, Y., Lin, Y., and Fu, J. S.: Mixing of dust with pollution on the transport path of Asian dust – Revealed from the aerosol over Yulin, the north edge of Loess Plateau, Sci. Total Environ., 409, 573–581, https://doi.org/10.1016/j.scitotenv.2010.10.032, 2011.

Wang, R., Balkanski, Y., Boucher, O., Bopp, L., Chappell, A., Ciais, P., Hauglustaine, D., Peñuelas, J., and Tao, S.: Sources, transport and deposition of iron in the global atmosphere, Atmos. Chem. Phys., 15, 6247–6270, https://doi.org/10.5194/acp-15-6247-2015, 2015.

Wang, X., Wei, W., Cheng, S., Zhang, H., and Yao, S.: Source estimation of SO_4^{2-} and NO_3^- based on monitoring-modeling approach during winter and summer seasons in Beijing and Tangshan, China, Atmos. Environ., 214, 116849, https://doi.org/10.1016/j.atmosenv.2019.116849, 2019.

Wang, Y., Hu, M., Hu, W., Zheng, J., Niu, H., Fang, X., Xu, N., Wu, Z., Guo, S., Wu, Y., Chen, W., Lu, S., Shao, M., Xie, S., Luo, B., and Zhang, Y.: Secondary Formation of Aerosols Under Typical High-Humidity Conditions in Wintertime Sichuan Basin, China: A Contrast to the North China Plain, J. Phys. Chem. A, 126, e2021JD034560, https://doi.org/10.1029/2021JD034560, 2021.

Watson, A. J. and Lefévre, N.: The sensitivity of atmospheric CO_2 concentrations to input of iron to the oceans, Tellus B Chem. Phys. Meteorol., 51, 453–460, https://doi.org/10.3402/tellusb.v51i2.16320, 1999.

Watson, A. J., Law, C. S., Van Scoy, K. A., Millero, F. J., Yao, W., Friederich, G. E., Liddicoat, M. I., Wanninkhof, R. H., Barber, R. T., and Coale, K. H.: Minimal effect of iron fertilization on sea-surface carbon dioxide concentrations, Nature, 371, 143–145, https://doi.org/10.1038/371143a0, 1994.

Weller, C., Tilgner, A., Bräuer, P., and Herrmann, H.: Modeling the Impact of Iron–Carboxylate Photochemistry on Radical Budget and Carboxylate Degradation in Cloud Droplets and Particles, Environ. Sci. Technol., 48, 5652–5659, https://doi.org/10.1021/es4056643, 2014.

Wong, J. P. S., Yang, Y., Fang, T., Mulholland, J. A., Russell, A. G., Ebelt, S., Nenes, A., and Weber, R. J.: Fine Particle Iron in Soils and Road Dust Is Modulated by Coal-Fired Power Plant Sulfur, Environ. Sci. Technol., 54, 7088–7096, https://doi.org/10.1021/acs.est.0c00483, 2020.

Wu, C. and Yu, J. Z.: Evaluation of linear regression techniques for atmospheric applications: the importance of appropriate weighting, Atmos. Meas. Tech., 11, 1233–1250, https://doi.org/10.5194/amt-11-1233-2018, 2018.

Wu, Y., Ge, X., Wang, J., Shen, Y., Ye, Z., Ge, S., Wu, Y., Yu, H., and Chen, M.: Responses of secondary aerosols to relative humidity and photochemical activities in an industrialized environment during late winter, Atmos. Environ., 193, 66–78, https://doi.org/10.1016/j.atmosenv.2018.09.008, 2018a.

Wu, Z., Wang, Y., Tan, T., Zhu, Y., Li, M., Shang, D., Wang, H., Lu, K., Guo, S., Zeng, L., and Zhang, Y.: Aerosol Liquid Water Driven by Anthropogenic Inorganic Salts: Implying Its Key Role in Haze Formation over the North China Plain, Environ. Sci. Technol. Lett., 5, 160–166, https://doi.org/10.1021/acs.estlett.8b00021, 2018b.

Xie, T., Lu, S., Zeng, J., Rao, L., Wang, X., Win, M. S., Zhang, D., Lu, H., Liu, X., and Wang, Q.: Soluble Fe release from iron-bearing clay mineral particles in acid environment and their oxidative potential, Sci. Total Environ., 726, 138650, https://doi.org/10.1016/j.scitotenv.2020.138650, 2020.

Xu, J., Chen, J., Zhao, N., Wang, G., Yu, G., Li, H., Huo, J., Lin, Y., Fu, Q., Guo, H., Deng, C., Lee, S.-H., Chen, J., and Huang, K.: Importance of gas-particle partitioning of ammonia in haze formation in the rural agricultural environment, Atmos. Chem. Phys., 20, 7259–7269, https://doi.org/10.5194/acp-20-7259-2020, 2020.

Yang, T., Chen, Y., Zhou, S., Li, H., Wang, F., and Zhu, Y.: Solubilities and deposition fluxes of atmospheric Fe and Cu over the Northwest Pacific and its marginal seas, Atmos. Environ., 239, 117763, https://doi.org/10.1016/j.atmosenv.2020.117763, 2020.

Zhang, G., Lin, Q., Peng, L., Yang, Y., Jiang, F., Liu, F., Song, W., Chen, D., Cai, Z., Bi, X., Miller, M., Tang, M., Huang, W., Wang, X., Peng, P. A., and Sheng, G.: Oxalate Formation Enhanced by Fe-Containing Particles and Environmental Implications, Environ. Sci. Technol., 53, 1269–1277, https://doi.org/10.1021/acs.est.8b05280, 2019.

Zhang, H., Li, R., Dong, S., Wang, F., Zhu, Y., Meng, H., Huang, C., Ren, Y., Wang, X., Hu, X., Li, T., Peng, C., Zhang, G., Xue, L., Wang, X., and Tang, M.: Abundance and Fractional Solubility of Aerosol Iron During Winter at a Coastal City in Northern China: Similarities and Contrasts Between Fine and Coarse Particles, J. Geophys. Res.-Atmos., 127, e2021JD036070, https://doi.org/10.1029/2021JD036070, 2022.

Zhang, Z., Boxall, C., and Kelsall, G. H.: Photoelectrophoresis of colloidal iron oxides 1. Hematite (α-Fe_2O_3), in: Colloids in the Aquatic Environment, edited by: Tadros, T. F., and Gregory, J., Elsevier, Oxford, 145–163, https://doi.org/10.1016/B978-1-85861-038-2.50014-0, 1993.

Zhou, M., Zhang, Y., Han, Y., Wu, J., Du, X., Xu, H., Feng, Y., and Han, S.: Spatial and temporal characteristics of $PM_{2.5}$ acidity during autumn in marine and coastal area of Bohai Sea, China, based on two-site contrast, Atmos. Res., 202, 196–204, https://doi.org/10.1016/j.atmosres.2017.11.014, 2018.

Zhou, Y., Zhang, Y., Griffith, S. M., Wu, G., Li, L., Zhao, Y., Li, M., Zhou, Z., and Yu, J. Z.: Field Evidence of Fe-Mediated Photochemical Degradation of Oxalate and Subsequent Sulfate Formation Observed by Single Particle Mass Spectrometry, Environ. Sci. Technol., 54, 6562–6574, https://doi.org/10.1021/acs.est.0c00443, 2020.

Zhu, X., Prospero, J. M., Savoie, D. L., Millero, F. J., Zika, R. G., and Saltzman, E. S.: Photoreduction of iron(III) in marine mineral aerosol solutions, J. Geophys. Res.-Atmos., 98, 9039–9046, https://doi.org/10.1029/93JD00202, 1993.

Zhu, X. R., Prospero, J. M., and Millero, F. J.: Diel variability of soluble Fe(II) and soluble total Fe in North African dust in the trade winds at Barbados, J. Geophys. Res.-Atmos., 102, 21297–21305, https://doi.org/10.1029/97JD01313, 1997.

Zhu, Y., Li, W., Lin, Q., Yuan, Q., Liu, L., Zhang, J., Zhang, Y., Shao, L., Niu, H., Yang, S., and Shi, Z.: Iron solubility in fine particles associated with secondary acidic aerosols in east China, Environ. Pollut., 264, 114769, https://doi.org/10.1016/j.envpol.2020.114769, 2020.

Zhuang, G., Yi, Z., Duce, R. A., and Brown, P. R.: Link between iron and sulphur cycles suggested by detection of Fe(n) in remote marine aerosols, Nature, 355, 537–539, https://doi.org/10.1038/355537a0, 1992.

Zuo, Y. and Hoigne, J.: Formation of hydrogen peroxide and depletion of oxalic acid in atmospheric water by photolysis of iron(III)-oxalato complexes, Environ. Sci. Technol., 26, 1014–1022, https://doi.org/10.1021/es00029a022, 1992.